

Strong anisotropic thermal conductivity of nanoporous silicon

Kyowon Kim^{a)} and Thomas E. Murphy

Institute for Research in Electronics and Applied Physics, University of Maryland, College Park, Maryland 20742, USA

(Received 21 July 2015; accepted 2 October 2015; published online 16 October 2015)

Nanoporous silicon is known to have a thermal conductivity that is orders of magnitude smaller than the bulk crystalline silicon from which it is formed. Even though the strong columnar microscopic structure of porous silicon indicates the possibility of highly anisotropic thermal properties, there have been no measurements. We report here an experimental investigation of this anisotropy. An analytical heat spreading model with 3ω thermal conductivity measurement method was used to derive both in-plane and cross-plane conductivities. Additionally, we describe a finite element analysis that supports the experimental measurements. Our measurements reveal that because of the nanoscale columnar nature of the material, the in-plane thermal conductivity of nanoporous silicon is 1–2 orders of magnitude smaller than the cross-plane thermal conductivity and 2–3 orders of magnitude smaller than that of crystalline silicon, making it comparable to the best thermal insulators available. © 2015 AIP Publishing LLC.

[<http://dx.doi.org/10.1063/1.4933176>]

I. INTRODUCTION

Nanoscale materials often exhibit optical, electrical, thermal, and mechanical properties that are significantly different from the bulk materials from which they are formed. The ability to control or tailor the macroscopic properties of these materials by engineering them at the nanoscale makes them attractive candidates for a variety of devices and applications. Nanoporous materials are especially promising for thermal insulation and isolation, because they provide the unique capability to use the microscopic structure to control or inhibit the flow of heat.^{1,2} Nanoporous silicon is of particular technological significance because it can be directly integrated atop conventional silicon microfabricated devices as a thermal, structural, or optical material.

Porous silicon is a composite of crystalline silicon interspersed with irregular nanoscale inclusions of air that are formed by electrochemical etching. The typical pore size formed in this process can be controlled by the dopant concentration and electrochemical current density but is typically 10–100 nm, and the porosity can range from 20% to 80%.^{3,4} Nanoporous silicon has unusual optical properties and can exhibit visible photoemission as a result of quantum confinement in the nanoscale structure. Its large surface area to volume ratio and permeability make porous silicon attractive for integrated optical or electrical sensors and for high-capacity batteries.^{5–8} Porous silicon is being investigated as a thermoelectric material, where because of its low thermal conductivity, it could outperform traditional thermoelectric materials such as Bi_2Te_3 .^{9,10}

Porous silicon is unique among nanocomposites because it remains monocrystalline during fabrication, which makes it mechanically compatible with the silicon substrates widely used in fabricating electrical and optical devices. Unlike traditional thermal insulation layers, porous silicon has a

coefficient of thermal expansion that is matched to the silicon substrate—an essential feature in any device that requires thermal cycling or cryogenic operation.

Figure 1 shows a top-down and cross-sectional scanning electron micrograph of a representative porous silicon material characterized here. The electrochemical etching process produces columnar pores that are preferentially oriented in the out-of-plane direction, causing anisotropy in the macroscopic properties. Infrared optical measurements reveal that nanoporous films have significant form birefringence and polarization-dependent loss.¹¹ Cross-plane and in-plane electrical measurements show a similar anisotropy in the conductivity of porous silicon.¹² Several techniques have been used to characterize the thermal conductivity of porous silicon, including the 3ω method, micro-Raman spectroscopy, scanning thermal microscopy, and photoacoustic measurements.^{13–18} In all cases, the thermal conductivity of porous silicon was shown to be in the range of $0.2\text{--}4\text{ W m}^{-1}\text{ K}^{-1}$ with the substrate resistivity of $0.01\text{--}0.2\ \Omega\ \text{cm}$, which is about 2 orders of magnitude smaller than that of crystalline silicon. The thermal conductivity tends to decrease as the resistivity increases. However, prior measurements have only

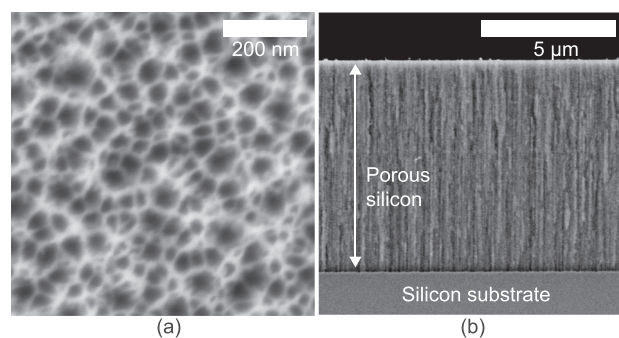


FIG. 1. Scanning electron micrograph of porous silicon. Top down (a) and cross section (b).

^{a)}Electronic mail: kyowon@umd.edu

characterized thermal conduction in the out-of-plane direction and often have relied on the assumption that the thermal properties are isotropic.

Direct measurement of the in-plane thermal conductivity requires fabricating samples with suspended film structure or encapsulating the film between insulating layers.^{19,20} Preparing free-standing porous silicon samples for those methods and with additional heating and sensing structures is extremely challenging process. Non-contact optical methods that do not require electrical heaters or sensors have been recently developed for thermal characterization, but these methods require extensive thermal and optical analysis and simulation to extract the thermal properties. Moreover, optical illumination has the potential to oxidize the nanoscale surfaces, which can modify the thermal properties.²¹

Here, we describe a new measurement to characterize the anisotropy of thermal conductivity in nanoscale porous silicon films. We use a modification of the tradition 3ω method that accounts for the anisotropy in the film, and by varying the ratio of the heater width to the film thickness, we show that it is possible to separately determine both independent tensor elements of the thermal conductivity. We further employ direct numerical simulation of the heat flow to match the experimental observations, thereby confirm our measurement of the in-plane thermal conductivity. The in-plane conductivity of nanoporous silicon is found to be $0.4\text{--}0.5\text{ W m}^{-1}\text{ K}^{-1}$, which is 1–2 orders of magnitude lower than the cross-plane conductivity. This extraordinarily low conductivity is obtained in a nanoscale material that is expansion matched and lattice-matched to the crystalline silicon substrates that are commonly used in electronic, optical, and thermal devices.

II. SAMPLE FABRICATION

Figure 2 shows the structure of the device used to study the thermal properties of porous silicon. The nanoporous

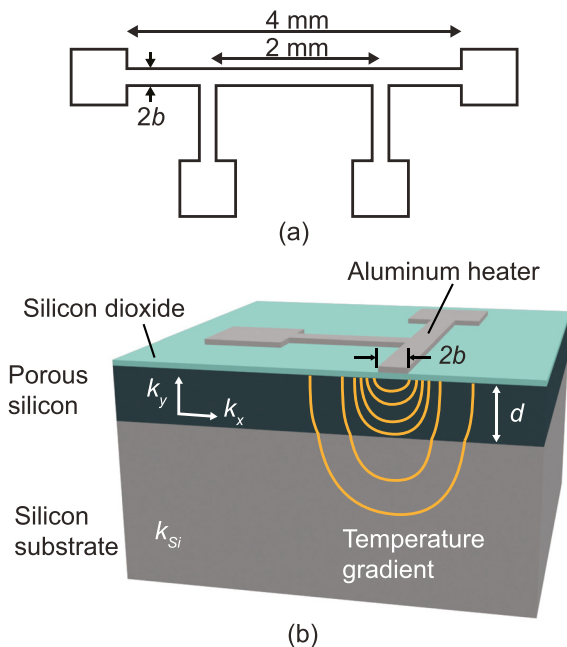


FIG. 2. (a) Top down view of aluminum heater. (b) Cross sectional view of 3ω measurement sample (not in scale).

film was prepared by electrochemical etching of p-type ($1\text{--}5\text{ m}\Omega\text{ cm}$) $\langle 100 \rangle$ silicon wafers with thickness of $500\text{ }\mu\text{m}$ in an electrolyte solution of hydrofluoric acid, water, and ethanol in 1:1:2 volume ratio. Note that the silicon wafer we used in this work has lower resistivity compared to previous porous silicon thermal conductivity studies. An electrochemical current of 38.3 mA/cm^2 was applied to produce a porous silicon layer with a volume porosity of 59.7%. Three different samples were produced, with layer thicknesses (d) of 5, 15, and $35\text{ }\mu\text{m}$. The etching current density was held constant throughout the duration of each etch, and from sample to sample, in order to ensure homogeneous and identical porosity and morphology for all film thicknesses. We therefore assumed that the effective thermal conductivity remains unchanged when the film thickness is changed from 5 to $35\text{ }\mu\text{m}$. This assumption was supported by optical reflectivity measurements, which indicated that all three film thicknesses have identical refractive indices. A 200 nm layer of SiO_2 was deposited on top of porous silicon layer using PECVD immediately after the etching process. The SiO_2 layer provides electrical insulation between the heating element and the porous film and silicon substrate, and inhibits oxidization of as-etched pore surface in the ambient air. The metal heating strip pattern was exposed with a custom-built scanning laser lithography system, using $1.3\text{ }\mu\text{m}$ of photoresist and subsequent thermal evaporation and liftoff of a 200 nm aluminum film.²² The lithography system avoids the use of a contact photomask mask that may otherwise damage the fragile porous silicon structure. The aluminum heating strips were 4 mm long and had widths ($2b$) of 4, 10, 16, 22, 28, and $34\text{ }\mu\text{m}$. The two contact pads at opposite ends of the heater were used to apply a sinusoidal heating current to the element, while the two intermediate pads allowed for sensing of the resulting voltage.

III. ANALYTICAL MODEL

The 3ω method uses a thin metal strip patterned atop a sample surface to serve as both a heater and thermometer, as shown in Figure 2. A sinusoidal electrical current $I(t)$ at frequency ω drives the resistive heating element and thereby produces a temperature change ΔT that is linearly related to $RI^2(t)$, which has a frequency component at 2ω . The resistance R of the device also depends on the temperature as

$$R = R_0(1 + \alpha\Delta T), \quad (1)$$

and therefore has both a DC and 2ω component. The measured voltage $V(t) = RI(t)$ then includes a frequency component at 3ω that can be precisely measured using a lock-in amplifier tuned to the third-harmonic of the driving frequency.

The 3ω component is caused solely by the thermally induced temperature variation and is directly proportional to the temperature rise of metal strip. The amplitude of the temperature oscillation $\Delta T_{2\omega}$ on the heater is related to the in-phase component of the measured amplitude $V_{3\omega}$ by

$$\Delta T_{2\omega} = \frac{2\Re\{V_{3\omega}\}}{\alpha I_{\omega} R_0}, \quad (2)$$

where I_ω is the RMS amplitude of the sinusoidal heating current, and α is the temperature coefficient of resistance described in Equation (1).^{23,24} In order to evaluate the role of anisotropy in the thermal conduction, we performed measurements of $V_{3\omega}$ with several different aspect ratios b/d while holding the areal thermal power density constant.

The temperature oscillation $\Delta T_{2\omega}$ can also be calculated by directly numerically solving the heat equation in two dimensions

$$\frac{\partial T}{\partial t} = \frac{1}{\rho C} \left[k_x \frac{\partial^2 T}{\partial x^2} + k_y \frac{\partial^2 T}{\partial y^2} \right], \quad (3)$$

where ρ and C represent density and heat capacity of porous silicon, k_x and k_y represent in-plane and cross-plane thermal conductivity of porous silicon, respectively. By comparing the numerical simulations with the experimentally determined temperature fluctuation given by Equation (2), it is possible to estimate the degree of anisotropy needed to best reproduce the experimental measurements.

Variations of the 3ω technique have been introduced depending on the sample configurations and film geometry. The ‘‘differential 3ω method’’ is commonly used to measure the cross-plane thermal conductivity of a thin film. In this method, the metal strip is much wider than the film thickness ($b \gg d$), so that the flow of heat into the substrate is primarily in the vertical direction, and the lateral heat spreading at the edges of the heater can be neglected. By performing measurements with and without the thin film present, one can determine the cross-plane thermal conductivity by modeling the film as a simple one-dimensional thermal resistance, from which one obtains the following simple relation:²⁵

$$k_y = \frac{\alpha d R_0^2 I_\omega^3}{4bL\mathbb{R} \{V_{3\omega} - V_{3\omega}^{(0)}\}}, \quad (4)$$

where V and $V_{3\omega}^{(0)}$ represent the measured third-harmonic RMS voltage amplitude with and without the thin film present, k_y is the cross-plane thermal conductivity. In practice, one typically measures $V_{3\omega}$ and $V_{3\omega}^{(0)}$ as a function of frequency ω and uses the difference between the curves to determine k_y .

When the metal strip width is comparable to or smaller than the film thickness, the heat diffusion in the in-plane direction cannot be ignored, and the induced temperature variation depends on both tensor components of the thermal conductivity and the ratio of b to d . Borca-Tasciuc *et al.* showed that in this case Equation (4) can be generalized to obtain

$$k_y = \frac{\alpha d R_0^2 I_\omega^3}{4bL\mathbb{R} \{V_{3\omega} - V_{3\omega}^{(0)}\}} F(\beta), \quad (5)$$

where the dimensionless function $F(\beta)$ is given by

$$F(\beta) = \frac{2}{\pi} \int_0^\infty \frac{\sin^2 \lambda \tanh(\lambda \beta)}{\lambda^3 \beta} d\lambda. \quad (6)$$

The argument β is given as

$$\beta = \sqrt{\frac{k_x d}{k_y b}}, \quad (7)$$

where k_x and k_y represent the in-plane and cross-plan thermal conductivity.²⁶

We note that $\lim_{\beta \rightarrow 0} F(\beta) = 1$, so that in the limit that either $d \ll b$ or $k_y \gg k_x$ Equation (5) approaches Equation (4). Because the function $F(\beta)$ is not invertible, the anisotropy factor must be determined by empirically finding the condition for which Equation (5) gives a consistent value for k_y for all possible values aspect ratios b/d considered in the experiments.

IV. MEASUREMENT

Figure 3 illustrates the experimental configuration of the 3ω measurement used to measure the thermal properties of porous silicon.²³ A dual-phase digital lock-in amplifier (Signal Recovery 7270) was used both as the current source and to measure the resulting third-harmonic voltage $V_{3\omega}$. The sinusoidal driving signal produced by the lock-in amplifier was found to contain a small amount of harmonic distortion at 3ω that interferes with the thermal signal to be measured. To eliminate this distortion, we connected a wire-wound variable resistor in series with the device under test and used the lock-in amplifier to record the voltage difference between the two resistors. The variable resistor was tuned to have a DC resistance that is matched to the sensing resistance of the device. This was accomplished by adjusting the resistance until the lock-in amplifier produces minimal response at the drive frequency ω . The variable resistor produces negligible heating in comparison to the device under test, and therefore its third-harmonic voltage component reflects only the harmonic distortion of the driving source, which is then subtracted when the two voltages are differentially detected in the lock-in amplifier. For each sample and for the reference substrate, the third harmonic voltage $V_{3\omega}$ was measured for frequencies ranging from 50 to 1000 Hz. In order to provide a comparison with finite-element time-domain simulations, separate measurements at 500 Hz were conducted for each sample, with the electrical power density adjusted in each case to achieve a fixed Joule heating density of $1 \times 10^5 \text{ W m}^{-2}$.

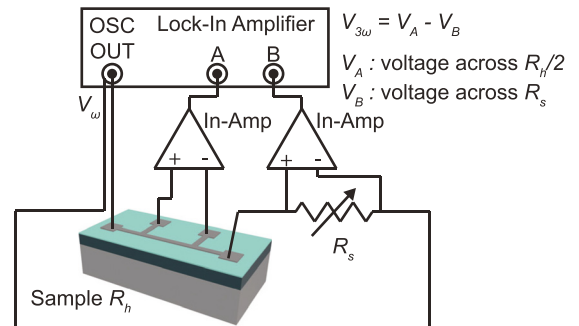


FIG. 3. Diagram of 3ω measurement system.

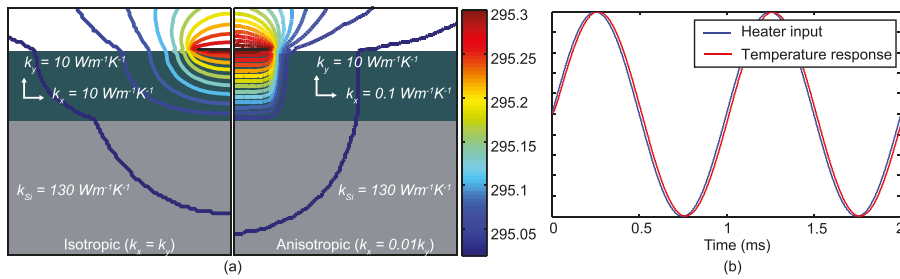


FIG. 4. (a) Comparison of heat spreading inside sample between isotropic and anisotropic case by numerical simulation. Temperature difference between the two adjacent contour lines is 0.02 K. (b) Normalized heat flow and temperature response of the heater. (Multimedia view) [URL: <http://dx.doi.org/10.1063/1.4933176.1>]

V. NUMERICAL SIMULATION

Thermal simulations were performed using a finite-element time-domain solver (CST Multiphysics Studio) to numerically calculate the temperature oscillation on the heater when excited by a sinusoidal heat flow at 1 kHz. We employed a two-dimensional computational window that encompassed one half of the cross-section of the heater structure. The mesh size was chosen to be approximately 1/10 of the narrowest heater width, and simulations confirmed that further reduction did not appreciably change the results. The thermal boundary condition at the mid-plane of the heater accounts for the symmetry of the structure, while all the other edges are defined to have open boundary conditions indicating that the material at the boundary extends to the infinity. The size of the computational domain was adjusted to ensure that the open boundaries did not affect the result.

The thermal conductivity of the substrate was taken to be $130 \text{ W m}^{-1} \text{ K}^{-1}$, which was obtained from separate measurements. Likewise, the cross-plane thermal conductivity of the porous silicon was taken to be $k_y = 10 \text{ W m}^{-1} \text{ K}^{-1}$, which was separately determined from large-area 3ω measurements. Thus, the only adjustable parameter in the simulations

was the anisotropy ratio $\gamma = k_x/k_y$. The heat flow density at the surface was held constant, to reflect the experimental conditions, and for each simulation the temperature variation at the surface was numerically determined, for comparison with the experimental measurements.

VI. RESULTS

Figure 4(a) (Multimedia view) shows the numerically simulated temperature distribution for $\gamma = 1$ (isotropic conductivity) and $\gamma = 0.01$. In the latter case, the strong thermal-conduction anisotropy causes the temperature gradient to be preferentially oriented in the vertical direction. Simulations were performed as a function of heater width $2b$, and for anisotropy ratios of $k_x/k_y = 1, 0.1,$ and 0.01 . Figure 4(b) shows a phase difference between the normalized heat flow and the temperature response of heater. In the 3ω measurement, the phase difference increases as driving frequency increases, but for the frequency considered here, the temperature is essentially in phase with the heat input. Figures 5(b)–5(d) plot the numerically simulated temperature amplitude as a function of the heater width, for porous silicon thicknesses of $d = 5, 15,$ and $35 \mu\text{m}$,

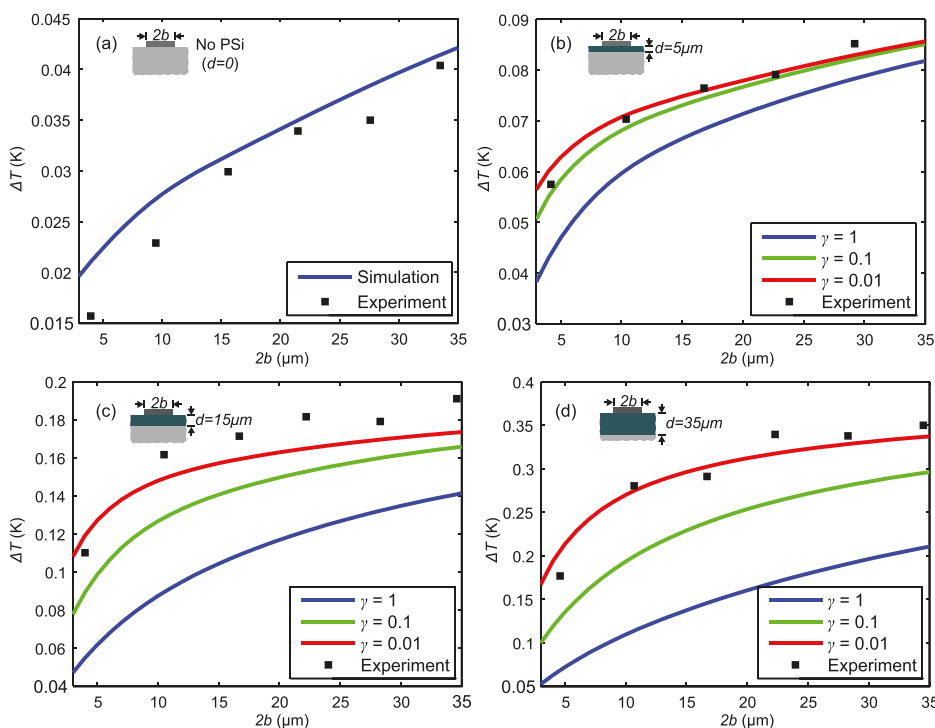


FIG. 5. Comparison between experimental data and numerical simulation for (a) no PSI film, (b) $5 \mu\text{m}$ PSI film, (c) $15 \mu\text{m}$ PSI film, and (d) $35 \mu\text{m}$ PSI film.

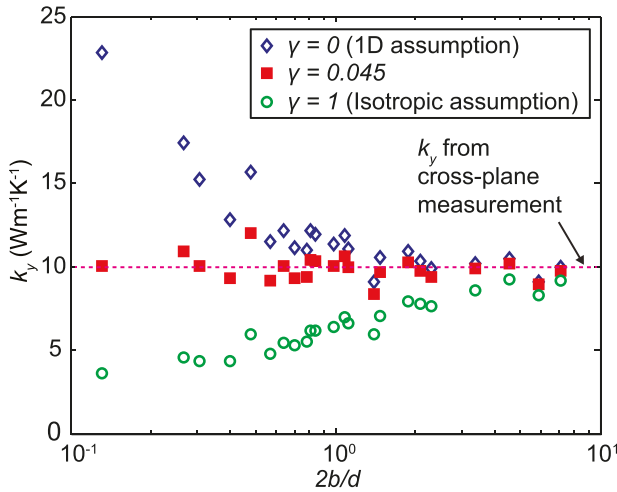


FIG. 6. k_y with $\gamma=0$ (1-D assumption), $\gamma=0.045$ and $\gamma=1$ (isotropic assumption).

along with the measured temperature amplitude calculated from Equation (2). Figure 5(a) shows the reference simulation when the porous film is absent, which agrees with the experimental observations, thus confirming the validity of the numerical simulation. For all cases, simulation results clearly show that $\Delta T_{2\omega}$ rises as γ decreases for given geometry. For the $5\ \mu\text{m}$ thick case (Figure 5(b)), the $\gamma=0.1$ and $\gamma=0.01$ are close together, because for this sample the geometric aspect ratio alone dictates that the conduction is primarily in the vertical direction, thus providing little sensitivity to the film anisotropy. By contrast, the $35\ \mu\text{m}$ case (Figure 5(d)) shows a clear dependence on the film anisotropy. Although the matching between experiment and simulation does not allow one to precisely determine the anisotropy factor γ , for the three cases considered, the simulations performed with $\gamma=0.01$ provide the closest agreement with the experimental data, indicating that the in-plane thermal conductivity is approximately 2 orders of magnitude smaller than the cross-plane conductivity.

We also considered the analytical model described by Equation (5), which gives an implicit expression for k_y if the anisotropy parameter γ and aspect ratio (b/d) are known. To find a self-consistent solution to this equation, we used the experimentally measured voltage differences $V_{3\omega} - V_{3\omega}^{(0)}$ to calculate k_y according to Equation (5), while assuming a constant value for the anisotropy factor γ . We then adjusted the value of γ in order to achieve the smallest variation in the computed values of k_y . The blue diamonds in Figure 6 show the computed value of k_y as a function of the aspect ratio b/d obtained by ignoring the thermal spreading, i.e., under the assumption that $\gamma=0$. In this case, the assumption of strictly one-dimensional heat flow leads to an overestimate k_y for low aspect ratio structures, but the result asymptotically approaches the correct measure in the limit that $b \gg d$. The green circles show the computed value of k_y obtained by assuming isotropic heat spreading ($\gamma=1$). In this case, Equation (5) underestimates cross-plane thermal conductivity, but again approaches the same asymptote in the limit $b \gg d$. We found that by assuming an anisotropy factor of

$\gamma=0.04-0.05$, Equation (5) predicts a consistent value of $10\ \text{W m}^{-1}\ \text{K}^{-1}$ for all of the samples measured, as indicated by the filled squares in Figure 6. The corresponding in-plane thermal conductivity is in the range $0.4-0.5\ \text{W m}^{-1}\ \text{K}^{-1}$, which is consistent with the numerical results, and on par with the best available thermal insulators.

Finally, we note that the pore size and porosity in porous silicon are known to depend on the dopant concentration and electrochemical current density. Although the measurements reported here were conducted for only one type of porous layer, we anticipate that the thermal anisotropy will also depend on the electrochemical etching parameters.

VII. CONCLUSION

In conclusion, porous silicon is an interesting material with directional nanoscale pores that exhibits low thermal conductivity. We measured the cross-plane and in-plane thermal conductivity of porous silicon thin film using a combination of the 3ω method and numerical simulation. Our measurements show that the in-plane thermal conductivity is a factor of 20 to 100 smaller than the cross-plane component, indicating that the columnar pores greatly inhibit the flow of heat in the direction perpendicular to the columns. These results show that nanoporous silicon can have exceptionally low in-plane thermal conductivity, which could have applications in thermoelectrics, bolometry, and energy storage.

ACKNOWLEDGMENTS

The authors would like to thank Ari Brown and Larry Hess from NASA Goddard Space Flight Center for helpful discussion. The microscopy and device fabrication were carried out at the University of Maryland Nanocenter. This work was partially supported by NSF CBET Award No. 0932673.

- ¹D. S. Smith, A. Alzina, J. Bourret, B. Nait-Ali, F. Pennec, N. Tessier-Doyen, K. Otsu, H. Matsubara, P. Elser, and U. T. Gonzenbach, *J. Mater. Res.* **28**, 2260 (2013).
- ²R. H. Tarkhanyan and D. G. Niarchos, *APL Mater.* **2**, 076107 (2014).
- ³R. L. Smith and S. D. Collins, *J. Appl. Phys.* **71**, R1 (1992).
- ⁴W. Theiß, *Surf. Sci. Rep.* **29**, 91 (1997).
- ⁵M. Thakur, M. Isaacson, S. L. Sinsabaugh, M. S. Wong, and S. L. Biswal, *J. Power Sources* **205**, 426 (2012).
- ⁶M. Ge, J. Rong, X. Fang, and C. Zhou, *Nano Lett.* **12**, 2318 (2012).
- ⁷C. Pacholski, *Sensors* **13**, 4694 (2013).
- ⁸F. A. Harraz, *Sens. Actuators, B* **202**, 897 (2014).
- ⁹J. Boor, D. S. Kim, X. Ao, M. Becker, N. F. Hinsche, I. Mertig, P. Zahn, and V. Schmidt, *Appl. Phys. A* **107**, 789 (2012).
- ¹⁰E. Hourdakis and A. G. Nassiopoulou, *Sensors* **13**, 13596 (2013).
- ¹¹V. Y. Timoshenko, L. A. Osminkina, A. I. Efimova, L. A. Golovan, P. K. Kashkarov, D. Kovalev, N. Künzner, E. Gross, J. Diener, and F. Koch, *Phys. Rev. B* **67**, 113405 (2003).
- ¹²S. Borini, L. Boarino, and G. Amato, *Appl. Phys. Lett.* **89**, 132111 (2006).
- ¹³G. Gesele, J. Linsmeier, V. Drach, J. Fricke, and R. Arens-Fischer, *J. Phys. D: Appl. Phys.* **30**, 2911 (1997).
- ¹⁴U. Bernini, S. Lettieri, E. Massera, and P. A. Rucco, *Opt. Laser Eng.* **39**, 127 (2003).
- ¹⁵U. Bernini, P. Maddalena, E. Massera, and A. Ramaglia, *Opt. Commun.* **168**, 305 (1999).
- ¹⁶S. Gomès, L. David, V. Lysenko, A. Descamps, T. Nychyporuk, and M. Raynaud, *J. Phys. D: Appl. Phys.* **40**, 6677 (2007).

- ¹⁷V. Lysenko, S. Périçon, B. Remaki, D. Barbier, and B. Champagnon, *J. Appl. Phys.* **86**, 6841 (1999).
- ¹⁸S. Périçon, V. Lysenko, B. Remaki, D. Barbier, and B. Champagnon, *J. Appl. Phys.* **86**, 4700 (1999).
- ¹⁹P. Ferrando-Villalba, A. F. Lopeandia, L. Abad, J. Llobet, M. Molina-Ruiz, G. Garcia, M. Gerbolès, F. X. Alvarez, A. R. Goñi, F. J. Muñoz-Pascual, and J. Rodríguez-Viejo, *Nanotechnology* **25**, 185402 (2014).
- ²⁰W. Jang, Z. Chen, W. Bao, C. N. Lau, and C. Dames, *Nano Lett.* **10**, 3909 (2010).
- ²¹M. N. Luckyanova, J. A. Johnson, A. A. Maznev, J. Garg, A. Jandl, M. T. Bulsara, E. A. Fitzgerald, K. A. Nelson, and G. Chen, *Nano Lett.* **13**, 3973 (2013).
- ²²K. Kim and T. E. Murphy, *Opt. Express* **21**, 19488 (2013).
- ²³D. G. Cahill, *Rev. Sci. Instrum.* **61**, 802 (1990).
- ²⁴C. Dames and G. Chen, *Rev. Sci. Instrum.* **76**, 124902 (2005).
- ²⁵D. G. Cahill, M. Katiyar, and J. R. Abelson, *Phys. Rev. B* **50**, 6077 (1994).
- ²⁶T. Borca-Tasciuc, A. R. Kumar, and G. Chen, *Rev. Sci. Instrum.* **72**, 2139 (2001).